

EFFECT OF PHOTODESORPTION ON SNOW LINE AT THE SURFACE OF OPTICALLY THICK CIRCUMSTELLAR DISKS AROUND HERBIG Ae/Be STARS

AKINORI OKA

Department of Earth and Planetary Sciences, Tokyo Institute of Technology, Ookayama, Meguro, Tokyo 152-8551, Japan

AKIO K. INOUE

College of General Education, Osaka Sangyo University, 3-1-1, Nakagaito, Daito, Osaka 574-8530, Japan

TAISHI NAKAMOTO

Department of Earth and Planetary Sciences, Tokyo Institute of Technology, Ookayama, Meguro, Tokyo 152-8551, Japan

AND

MITSUHIKO HONDA

Department of Information Science, Kanagawa University, 2946, Tsuchiya, Hiratsuka, Kanagawa 259-1293, Japan

Draft for ApJ

ABSTRACT

We investigate the effect of photodesorption on the snow line position at the surface of a protoplanetary disk around a Herbig Ae/Be star, motivated by the detection of water ice particles at the surface of the disk around HD142527 by Honda et al. For this aim, we obtain the density and temperature structure in the disk with a 1+1D radiative transfer and determine the distribution of water ice particles in the disk by the balance between condensation, sublimation, and photodesorption. We find that photodesorption induced by the far-ultraviolet radiation from the central star depresses the ice-condensation front toward the mid-plane and pushes the surface snow line outward significantly when the stellar effective temperature exceeds a certain critical value. This critical effective temperature depends on the stellar luminosity and mass, the water abundance in the disk, and the yield of photodesorption. We present an approximate analytic formula for the critical temperature. We separate Herbig Ae/Be stars into two groups on the HR diagram according to the critical temperature; one is the disks where photodesorption is effective and from which we may not find ice particles at the surface, and the other is the disks where photodesorption is not effective. We estimate the snow line position at the surface of the disk around HD142527 to be 100–300 AU which is consistent with the water ice detection at > 140 AU in the disk. All results depend on the dust grain size by a complex way and this point requires more work in future.

Subject headings: methods: numerical — protoplanetary disks — radiative transfer — stars: individual (HD142527)

1. INTRODUCTION

In a protoplanetary disk, there is the so-called snow line which is defined as the inner boundary of the ice-condensing region (e.g., Hayashi 1981). Beyond the snow line, the surface mass density of solid materials is enhanced due to condensation of water ice, and hence, the formation efficiency of large gaseous and icy planets is expected to be enhanced. Thus, the snow line plays a very important role in the planet formation.

In spite of its importance, no one has detected the snow line position in a circumstellar disk so far. This is because the snow line is usually located close to the central star ($R \lesssim 10$ AU), where the spacial resolving power of current facilities is limited, and the disk is optically too thick to see through. On the other hand, the presence of water ice in circumstellar disks have already been detected (e.g., Malfait et al. 1999; Terada et al. 2007; Honda et al. 2009). Terada et al. (2007) observed scattered radiation from an *edge-on* disk and detected an absorption feature of water ice at $3 \mu\text{m}$ in it. However,

their observations give no information about the position of the snow line along the line of sight. Honda et al. (2009) observed scattered light from the surface of an *face-on* disk and detected the $3 \mu\text{m}$ absorption feature by icy dust particles at $R \gtrsim 140$ AU. They could estimate the dust size as $\sim 1 \mu\text{m}$ by using a color diagram method proposed by Inoue et al. (2008). While Honda et al. (2009) could not detect the snow line position, their method holds a potential to achieve it due to a high spatial resolution of their detection technique.

Although an important factor for the planet formation is the snow line position at the mid-plane, detecting the snow line at the disk surface will be a first step because the disk surface is easily observed. The surface snow line is connected to the mid-plane snow line through a 2D structure of the ice-condensing region (e.g., Davis 2005; Oka, Nakamoto & Ida 2011). If one knows the mechanism which determines the 2D structure of the snow line, one may convert the surface snow line into the mid-plane snow line.

The main difference between the interior and the surface of protoplanetary disks is that the latter is exposed

to ultra-violet (UV) radiation from the central star and the interstellar radiation field. This UV radiation may affect the distribution of water ice at the disk surface. Indeed, it has been proposed that a non-thermal desorption process is necessary for explaining the observed high abundance of gas-phase water molecules in cold outer regions of circumstellar disks and molecular clouds (e.g., Dominik et al. 2005; Hollenbach et al. 2009). A probable mechanism responsible for such a non-thermal desorption of water molecules is the photodesorption (or photospattering) process caused by far-UV (FUV) radiation. The photodesorption process has been recently studied theoretically and experimentally (e.g., Westley et al. 1995a,b; Andersson et al. 2006; Andersson & van Dishoeck 2008; Öberg et al. 2009; Hama et al. 2010).

Öberg et al. (2009) experimentally studied the photodesorption process and derived the photodesorption yield as a function of ice temperature and thickness of the ice layer. According to their results, the photodesorption yield with ice temperature T and thickness of the ice layer larger than 8 mono layers is $Y_{\text{pd}}(T, x > 8) = 10^{-3}(1.3 + 0.032T)$ UV photon $^{-1}$, where x is the ice thickness scaled by a mono layer. They then carried out a numerical simulation about the distribution of gas phase H_2O in a protoplanetary disk around a Herbig Ae/Be star, taking into account adsorption and thermal desorption processes on dust grains, and the photodesorption process, and found that photodesorption reduced the H_2O ice abundance in the disk surface by orders of magnitudes.

Grigorieva et al. (2007) also showed theoretically that the presence of icy dust particles in a debris disk around a Herbig Ae/Be star is affected by the photodesorption process. The environment of the surface of protoplanetary disks such as one observed by Honda et al. (2009) may be similar to that of debris disks, and hence the position of the surface snow line would be affected by the photodesorption process.

Recently, observations of water vapor in protoplanetary disks show a rapid progress with *Spitzer Space Telescope* and *Herschel Space Observatory* as well as large ground-based telescopes (e.g., Pontoppidan et al. 2010; Sturm et al. 2010; van Kempen et al. 2010; Bergin et al. 2010; Fedele et al. 2011). There is lack of hot and warm vapor traced by near- and mid-infrared observations in disks around Herbig Ae/Be stars, whereas such vapor was often found in disks around T Tauri stars (Pontoppidan et al. 2010; Fedele et al. 2011). A difference of photochemistry is suggested as a cause of this difference. In Herbig Ae/Be disks, H_2O molecules (photo)desorbed from icy grains may be photodissociated by strong UV radiation. On the other hand, Sturm et al. (2010) and van Kempen et al. (2010) detected cool water vapor in far-infrared observations in Herbig Ae/Be disks, suggesting incomplete photodissociation in the outer part of the disks. More interestingly, Bergin et al. (2010) reported no detection of cold water vapor in submillimetre in a T Tauri disk and suggested that photodesorption was less efficient than theoretically expected. In any case, more works about photodesorption and photodissociation in protoplanetary disks are required to depict a full picture of the photochemical evolution in the disks. In particular, less efficient pho-

to-desorption suggested by Bergin et al. (2010) should be tested also in Herbig Ae/Be stars.

In this study, we numerically investigate the effect of the photodesorption process induced by the FUV radiation from the central star and the interstellar radiation field on the surface snow line position in circumstellar disks. We focus on Herbig Ae/Be disks where photodesorption is effective as expected, while the parameter space explored in this paper also covers T Tauri disks. The goal is to uncover what the determining process of the snow line position at a disk surface is. We omit photodissociation in this paper, but in fact, we find that this process is much slower than photodesorption (see §4.3.1).

This paper is organized as follows. In §2, we describe our model for obtaining the distribution of icy dust particles in a Herbig Ae/Be disk with photodesorption. In §3, we show effects of photodesorption on the position of the surface snow line and the dependence of the results on the stellar parameters. In §4, we consider an implication of our results for observations, derive an analytic formula of the critical stellar effective temperature for an efficient photodesorption, and discuss effects of some processes omitted in our calculations. Finally, we summarize this paper in §5.

2. MODEL

2.1. Disk structure

We consider a flared but geometrically-thin and optically-thick disk revolving around a central star in Kepler velocity. We assume that the disk is axi-symmetric about the rotational axis and plane-symmetric about the mid-plane. We adopt a coordinate system (R, Z) , where R and Z are the radial distance from the central star and the vertical height from the disk mid-plane, respectively. The central star sits on the origin of the coordinate.

We assume that the radial distribution of the surface density of the disk is a power law distribution (e.g., Hayashi 1981) as

$$\Sigma(R) = \Sigma_{1\text{AU}} \left(\frac{R}{1\text{AU}} \right)^{-p}, \quad (1)$$

where $\Sigma_{1\text{AU}}$ is the surface density at $R = 1\text{AU}$ and p is the power-law index describing the radial density distribution. We assume $\Sigma_{1\text{AU}} = 1700 \text{ g cm}^{-2}$ and $p = 1.5$ (Hayashi 1981) throughout this paper. The disk is assumed to be in the hydrostatic equilibrium vertically, and heated by the irradiation by the central star. The temperature and density structures of the disk are numerically solved by the 1+1D radiative transfer method described by Dullemond et al. (2002). We assume that temperatures of dust and gas are always same. Unlike Dullemond et al. (2002), we consider isotropic scattering of both stellar and diffuse radiations according to Inoue et al. (2009) and Oka, Nakamoto & Ida (2011). The details of the calculation are described in Appendix A (see also Oka, Nakamoto & Ida 2011). Note that we assume that the grazing angle (β) of the stellar radiation incident on the disk surface is uniformly 0.05 throughout the disk for simplicity. This is fairly artificial but it was very difficult to determine both the grazing angle and the ice abundance simultaneously in our 1+1D disk with scattering by an iteration scheme because of very slow

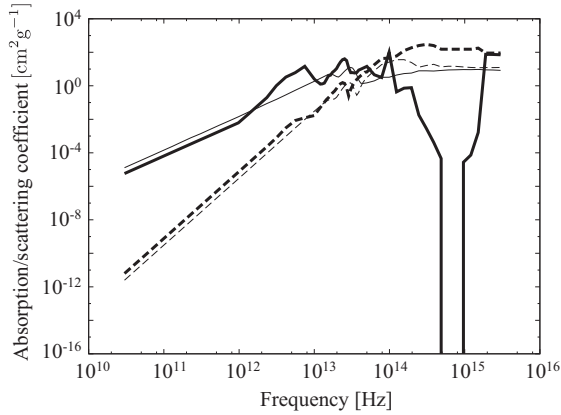


Figure 1. Absorption and scattering coefficients of the disk gas containing $1 \mu\text{m}$ -sized silicate and water ice particles adopted in our calculation. These coefficients are taken from Miyake & Nakagawa (1993). Note that all the water molecules are contained in the icy dust particles. The thick and thin curves represent the coefficients by icy and silicate dust particles, respectively. The solid and dashed curves represent the absorption and scattering coefficients, respectively.

convergence. The mean molecular weight of the disk gas is assumed to be 2.3.

Although we fix global parameters of the disk such as $\Sigma_{1\text{AU}}$, p , and β , it would not affect the results presented in this paper very much when discussing the disk surface where the radiative transfer effect is negligible and the physical condition is determined almost locally. This enables us to derive an analytic formula describing the numerical results in §4.2, while the absolute scaling may be affected slightly.

2.2. Dust opacity

A very important factor for determining the structure and the radiation field in the disk is the optical property of the disk. This is mainly determined by the absorption and scattering processes by dust particles. The gas opacity is negligible for the radiation considered in this paper, except for Ly α photons. We omit gas opacity throughout this paper for simplicity, whereas an importance of Ly α transfer was suggested (Fogel et al. 2011; Bethell & Bergin 2011). It is still reasonable when discussing the disk surface where the transfer effect is small.

We consider only pure crystalline silicate and pure crystalline water ice particles floating in the disk gas as dust. These particles are assumed to be spherical with a fixed uniform size to avoid complexity. Here we assume $1 \mu\text{m}$ -sized particles as found in the HD142527 disk by Honda et al. (2009), but the effect of the grain size is discussed in §4.3.4. The mass fractions of silicate and water to the disk gas are assumed to be 0.0043 and 0.0094, respectively, (Miyake & Nakagawa 1993) and uniform throughout the disk. This water abundance corresponds to the number fraction of H_2O molecules relative to all gas particles in the disk as $X_{\text{total}}^{\text{H}_2\text{O}} = 1.2 \times 10^{-3}$ which is the maximum fraction of water vapor.¹ The absorption and scattering coefficients of silicate and water ice particles are also taken from Miyake & Nakagawa (1993). The coefficients for $1 \mu\text{m}$ -sized particles for a

¹ The H_2O abundance in Miyake & Nakagawa (1993) was not taken into account the recent downward revision of O abundance (Asplund et al. 2009).

unit disk mass are shown in Figure 1.

2.3. Ice abundance

We evaluate the abundance of water ice in the disk by the balance between changing rates of the ice dust radius due to condensation \dot{s}_{con} , sublimation \dot{s}_{sub} , and photodesorption \dot{s}_{pd} ;

$$\dot{s}_{\text{sub}}(T) + \dot{s}_{\text{con}}(T, X_{\text{vapor}}^{\text{H}_2\text{O}}) + \dot{s}_{\text{pd}} = 0, \quad (2)$$

where $X_{\text{vapor}}^{\text{H}_2\text{O}}$ is the number fraction of water vapor of the disk medium and T is the dust (and gas) temperature. The rates are evaluated by the formulas from Grigorieva et al. (2007) (see Appendix B). The dust temperature T is obtained by the radiative transfer calculation described in §2.1 and Appendix A.

The number fraction of water vapor $X_{\text{vapor}}^{\text{H}_2\text{O}}$ is determined as equation (2) is fulfilled. Then, the number fraction of H_2O in water ice to the disk gas $X_{\text{ice}}^{\text{H}_2\text{O}}$ is given by the residual of the subtraction of $X_{\text{vapor}}^{\text{H}_2\text{O}}$ from the total number fraction of H_2O $X_{\text{total}}^{\text{H}_2\text{O}}$. On the other hand, if $\dot{s}_{\text{sub}} + \dot{s}_{\text{con}} + \dot{s}_{\text{pd}} < 0$ with $X_{\text{vapor}}^{\text{H}_2\text{O}} = X_{\text{total}}^{\text{H}_2\text{O}}$, water ice does not condense and $X_{\text{ice}}^{\text{H}_2\text{O}} = 0$. Using $X_{\text{total}}^{\text{H}_2\text{O}}$ and $X_{\text{ice}}^{\text{H}_2\text{O}}$, the mass ratio of water ice to the total water abundance x_{ice} is given by

$$x_{\text{ice}} = \frac{X_{\text{ice}}^{\text{H}_2\text{O}}}{X_{\text{total}}^{\text{H}_2\text{O}}}. \quad (3)$$

Then, the absorption and scattering coefficients of a unit disk mass containing dust particles, κ_{abs} and κ_{sca} are given by

$$\kappa_{\text{abs}} = \kappa_{\text{sil,abs}} + x_{\text{ice}}\kappa_{\text{ice,abs}}, \quad (4)$$

$$\kappa_{\text{sca}} = \kappa_{\text{sil,sca}} + x_{\text{ice}}\kappa_{\text{ice,sca}}, \quad (5)$$

where $\kappa_{\text{sil,abs}}$, $\kappa_{\text{sil,sca}}$, $\kappa_{\text{ice,abs}}$, and $\kappa_{\text{ice,sca}}$ are the absorption and scattering coefficients of silicate and water ice dust particles by Miyake & Nakagawa (1993), respectively ($\kappa_{\text{ice,abs}}$ and $\kappa_{\text{ice,sca}}$ are the coefficients in the case where all the water molecules are condensed as icy dust particles). Since x_{ice} itself affects the disk structure through the radiative transfer, we solve x_{ice} and the disk structure iteratively to obtain consistent solutions of them.

2.4. Stellar and interstellar FUV radiation

We consider three sources of UV radiation: the stellar photosphere, an excess stellar radiation (probably caused by an accretion shock), and the interstellar radiation field. The stellar photospheric radiation is treated in the radiative transfer code described in §2.1 and Appendix A. We assume the spectrum to be a Planck function. The transfer of the other two radiation sources are treated as described in the subsequent paragraphs. As found in §2.5 and §3.2, however, the two sources have a very weak effect on the position of the surface snow line. The heating by the two sources is taken into account in equation (A8) in addition to that of the photospheric radiation.

An excess FUV radiation is often observed in T Tauri stars, while the photospheric radiation is dominant in Herbig stars (e.g., Valenti et al. 2003). Nevertheless we

consider the excess radiation for discussions of the dependence of the stellar effective temperature in §3.2. We assume the excess FUV luminosity to be a fraction of 10^{-3} to the bolometric luminosity of the photosphere (L_*) as observed in T Tauri stars (Herczeg et al. 2004). This reproduces the observational trend that the excess relative to the photospheric radiation is less important for earlier spectral type. Observations show that the excess FUV radiation is dominated by Ly α photons (Herczeg et al. 2004). We assume that the excess radiation consists only of Ly α photons for simplicity. However, we omit any scattering of the Ly α photons (see §2.2) although the resonant scattering of the photons is important in the sub-surface layer of the disk (Fogel et al. 2011; Bethell & Bergin 2011). The Ly α assumption is only affects the calculation of the optical depth in the disk and the photon number flux. Consequently, the excess FUV radiation flux in the disk can be obtained as

$$F_{\text{FUV,excess}}(R, Z) = F_{\text{FUV,excess},0}(R) \exp(-\tau_{\text{FUV}}(Z)/\beta), \quad (6)$$

where $F_{\text{FUV,excess},0}(R) = 10^{-3} L_*/(4\pi R^2)$ is the incident excess FUV flux from the central star at the radius R for no dust case, $\tau_{\text{FUV}}(Z)$ is the absorption optical depth at the FUV (Ly α) wavelength measured along the Z -axis from $(R, +\infty)$ to (R, Z) , and β is the grazing angle for the stellar radiation.

We also consider the FUV radiation from the interstellar field. We adopt an average FUV radiation flux from Habing (1968). The FUV flux is evaluated by assuming that it penetrates into the disk parallel to the Z -axis:

$$F_{\text{FUV,is}}(R, Z) = F_{\text{FUV,is},0} \exp(-\tau_{\text{FUV}}(Z)), \quad (7)$$

where $F_{\text{FUV,is},0}(R, Z)$ is the incident interstellar FUV radiation flux and is set to be $1.6 \times 10^{-3} \text{ erg cm}^{-2} \text{ s}^{-1}$. The interstellar FUV radiation is also assumed to be consisted only of Ly α photons as the stellar excess FUV. This is simply in order to treat the two additional FUV radiation sources homogeneously, whereas the interstellar radiation may be described by a Planck function or a power-law function made by a combination of Planck functions with various temperatures.

2.5. Examples of disk vertical structure

Figure 2 shows examples of the vertical structure of two annuli at $R = 10 \text{ AU}$ (left-hand tandem panels) and 100 AU (right-hand tandem panels) around a central star with the effective temperature $T_* = 5000 \text{ K}$, the luminosity $L_* = 10 L_\odot$, and the mass $M_* = 1 M_\odot$. The top panels show the temperature structure along the disk vertical axis. The middle panels show the changing rates of the grain size by condensation (double-dot-dashed line), sublimation (dotted line), and photodesorption (solid line). We also show the changing rates by photodesorption due to stellar (photospheric and excess) radiation (dashed line) and due to interstellar radiation (dot-dashed line). The bottom panels show the ice condensation fraction.

In both annuli, condensation is rapid near the mid-plane and virtually all water is in ice. As the temperature increases (and the density decreases) along the vertical height, condensation becomes slower and slower. On the other hand, sublimation and photodesorption become suddenly effective beyond a certain height. Then, the ice condensation front is formed at a height where

condensation balances with sublimation or photodesorption. In the $R = 10 \text{ AU}$ case, sublimation is faster than photodesorption at the front, and then, the balance is established between condensation and sublimation. On the other hand, in the $R = 100 \text{ AU}$ case, sublimation is more than ten orders of magnitudes slower than photodesorption because of a low temperature. Thus, condensation balances with photodesorption.

Photodesorption by stellar FUV radiation always dominates that by interstellar FUV radiation at the disk surface because of a much stronger flux of the former radiation. However, the latter dominates the former at a sub-surface layer. This is caused by the different incident angles of the two radiations; the stellar radiation enters the disk with a small angle against the surface (i.e. grazing angle β) and the penetration depth becomes shallow, whereas the interstellar radiation enters the disk vertically and reaches a deeper layer. When discussing the surface snow line, we conclude that the interstellar radiation hardly contributes to the determination of the surface snow line. Therefore, we omit the contribution by the interstellar FUV radiation in the remaining part of this paper.

2.6. Definition of the surface snow line

Let us define the position of the surface snow line, here. We consider the method observing the surface snow line by using the $3 \mu\text{m}$ H₂O ice absorption feature in the scattered light proposed by Inoue et al. (2008) theoretically and attempted by Honda et al. (2009) observationally. The $3 \mu\text{m}$ scattered light comes from the layer to which the optical depth for the $3 \mu\text{m}$ radiation from the central star is about unity. Therefore, we define the layer as the disk ‘surface’ or ‘ $3 \mu\text{m}$ surface’ in this paper. Next, we consider the ice-condensation front in the (R, Z) -plane. Without the accretion viscous heating, the temperature decreases along the radial coordinate R and increases along the vertical coordinate Z . Thus, the ice-condensation front becomes lower Z for smaller R and higher Z for larger R (see Fig. 3). Then, there may be a cross-point between the $3 \mu\text{m}$ surface and the ice-condensation front. If we observe a disk with the scattered light, we will observe the $3 \mu\text{m}$ feature only from the outside of the cross-point. Therefore, we define the cross-point as the surface snow line in this paper. Namely, the surface snow line in this paper is the snow line which would be observed by the $3 \mu\text{m}$ scattered light.

3. RESULT

3.1. Structure of the ice-condensation front and the surface snow line

Figure 3 shows the ice-condensation front (solid curve) and the surface snow line position (vertical tick) in a disk around a star with the effective temperature $T_* = 6000 \text{ K}$, the luminosity $L_* = 10 L_\odot$, and the mass $M_* = 1 M_\odot$. The layers of $\tau_{3\mu\text{m}} = 0.1, 1, \text{ and } 10$ are also shown as the dotted curves, where $\tau_{3\mu\text{m}}$ is the optical depth at the wavelength $3 \mu\text{m}$ from the central star. The layer of $\tau_{3\mu\text{m}} = 1$ is the $3 \mu\text{m}$ surface of the disk. We also show the pressure scale-height calculated by the mid-plane temperature as the dashed curve in each panel.

Comparing the panel (a), where photodesorption is omitted, with the panel (b), where the process works, we

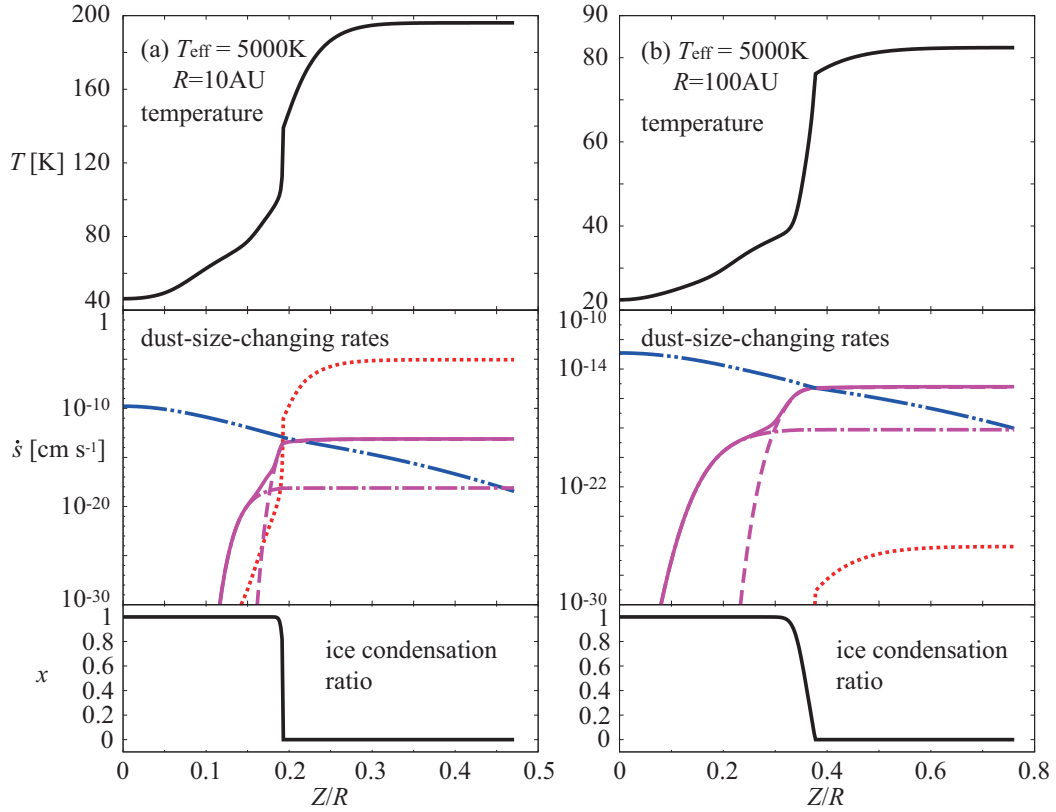


Figure 2. Vertical profiles of disk annuli with the radius of (a) 10 AU and (b) 100 AU. The stellar effective temperature of 5000 K, luminosity of $10 L_{\odot}$, and mass of $1 M_{\odot}$ are assumed. The top panels show the temperature profiles. The middle panels show the profiles of the changing rates of the grain size \dot{s} due to condensation (double-dot-dashed), sublimation (dotted), and photodesorption (solid). The dashed and dot-dashed curves represent the rates due to photodesorption induced by the stellar (photospheric and excess) FUV luminosity and the interstellar FUV radiation, respectively. The bottom panels show the profile of the ice condensation fraction x . The horizontal axis represents altitudes from the disk mid-plane scaled by the radius of the annuli.

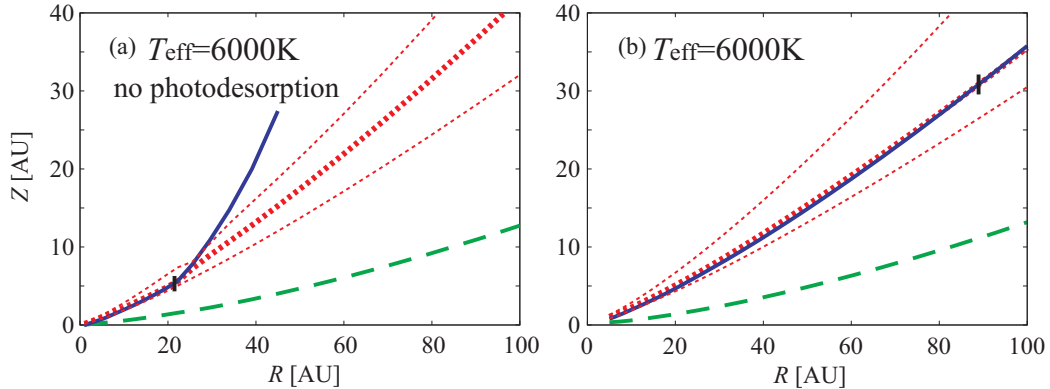


Figure 3. The structure of the ice-condensation front in a circumstellar disk. The horizontal and vertical axes represent the distance from the central star R and the height from the mid-plane Z in astronomical unit, respectively. The panels (a) and (b) are the cases without and with photodesorption, respectively. The stellar parameters assumed are the effective temperature of 6000 K, the luminosity of $10 L_{\odot}$ and the mass of $1 M_{\odot}$. The dust particle size is assumed to be $1.0 \mu\text{m}$. The solid curve represents the condensation front below which water ice particles exist. The dashed curve represents the pressure scale height of the disk medium. The upper (thin), middle (thick), and lower (thin) dotted curves represent layers at which the optical depth at wavelength $3 \mu\text{m}$ from the central star becomes 0.1, 1 ($3 \mu\text{m}$ 'surface'), and 10, respectively. The vertical tick indicates the cross-point between the ice-condensation front and the $3\text{-}\mu\text{m}$ disk surface, i.e. the surface snow line position.

find that photodesorption wipes out water ice particles above the disk surface and the ice-condensation front almost coincides with the surface throughout the disk. The position of the surface snow line (i.e. the cross-point of the ice-condensation front and the $3\ \mu\text{m}$ surface) shifts outward by a factor of about 4 for this case. As shown later (Figs. 4 and 5), the radial shift becomes larger and larger as the effective temperature increases. Therefore, photodesorption is very important to determine the position of the surface snow line for Herbig stars.

3.2. Stellar parameter dependence of the surface snow line

In this section, we examine the dependence of the surface snow line position R_{snow} on the stellar effective temperature T_* , the luminosity L_* , and the mass M_* . In this calculation, we omit opacity of water ice particles for the computational cost. This simplification gives 20–30% smaller radius of the surface snow line position as shown in Figure 4. This relatively small difference is probably caused by an offset of two opposite effects; (1) A smaller opacity in the case without ice opacity results in a higher temperature in the disk interior (i.e. a higher pressure height found in Fig. 4) and also a higher surface height defined by $\tau_{3\mu\text{m}} = 1$ (as also found in Fig. 4). However, this leads a smaller density at the surface, and then, the condensation rate becomes slower and the surface snow line shifts outward. (2) The smaller opacity also results in a larger column density from infinity to the surface in order to account for $\tau_{3\mu\text{m}} = 1$ at the surface. It leads a lower surface height and a larger density at the surface. Then, the condensation rate becomes faster, and the surface snow line shifts inward. This second effect exceeds the first effect in the cases shown in Figure 4. In any case, the omission of the ice opacity does not change the mechanism determining the surface snow line position.

3.2.1. Effective temperature

As found in Figure 4, the position of the surface snow line strongly depends on the stellar effective temperature; as the temperature increases, the surface snow line shifts outward greatly and eventually disappears. Figure 5 shows this dependence more in detail for the cases with $M_* = 1 M_\odot$ and $L_* = 1 L_\odot$ and $10 L_\odot$. The dot-dashed curves indicate the cases without photodesorption, i.e., R_{snow} is determined by the balance between sublimation and condensation. On the other hand, the dotted curves are the cases without sublimation, i.e., R_{snow} is determined by the balance between photodesorption and condensation. The solid curves are the cases with all the three processes. The dashed curves are same as the solid curves but without the stellar excess FUV (see §2.4).

For the sublimation–condensation cases (dot-dashed curves), R_{snow} is about 7 or 25 AU and almost independent of T_* , but depends on L_* as $R_{\text{snow}} \propto L_*^{1/2}$. This is because the gas temperature for the sublimation–condensation balance is almost constant at ~ 100 K at the disk surface where the dust temperature is determined only by bolometric flux (i.e. $\propto L_*/R^2$) and not the spectrum (see also §4.2). For the photodesorption–condensation cases (dotted curves), R_{snow} strongly depends on T_* as $R_{\text{snow}} \propto T_*^{12}$. This strong dependence comes from the T_* dependence in the FUV photon num-

ber flux (see §4.2). It also depends on L_* as $R_{\text{snow}} \propto L_*^2$ which is different from the sublimation–condensation case.

When all the three processes are taken into account (solid curves), R_{snow} traces the sublimation–condensation case for lower T_* and the photodesorption–condensation case for higher T_* . In other words, the mechanism determining R_{snow} is the sublimation–condensation balance for lower T_* and the photodesorption–condensation balance for higher T_* . We here define a critical temperature T_c as T_* at the intersection point between the two curves of the sublimation–condensation case and the photodesorption–condensation case. If $T_* > T_c$, photodesorption is efficient and the surface snow line moves to the outermost part of the disk or disappears. Thus, T_c is an indicator for judging the possibility to detect the $3\ \mu\text{m}$ water ice absorption feature in the disk scattered radiation (see §4.1).

If we compare the dashed curves (the cases without the excess FUV) with the solid curves, we can see the effect of the stellar FUV excess on the surface snow line. Although it is still uncertain how strong the FUV excess is, we assume that the FUV excess accounts for only 0.1% of L_* (§2.4). We find an effect of the FUV excess in the $L_* = 10 L_\odot$ case. If the FUV excess is stronger than this level, we should take it into account in order to determine the position of the surface snow line correctly.

3.2.2. Stellar luminosity

Figure 6 shows R_{snow} as a function of T_* with various L_* s and $M_* = 1 M_\odot$. It is seen that R_{snow} shifts outward as L_* increases. This is because both the FUV radiation flux from the central star and the temperature in the disk increase as L_* increases. It is also seen that the critical temperature T_c becomes lower as L_* increases. The dependence is approximately $T_c \propto L_*^{-1/8}$ (see §4.2).

3.2.3. Stellar mass

Figure 7 shows R_{snow} as a function of T_* with $L_* = 10 L_\odot$ and various M_* s. It is seen that the critical temperature T_c becomes higher as M_* increases. This is because the condensation rate is approximately proportional to the square root of M_* ; the condensation rate depends linearly on the gas pressure with the assumption of uniformly constant number fraction of water molecules in the whole disk, and the gas pressure depends approximately linearly on the square root of M_* (see eqs. A1–A3, and also §4.2).

4. DISCUSSION

4.1. Implications for the observation

In this section, we discuss the effect of photodesorption on observing the surface snow line. As proposed by Inoue et al. (2008), we can resolve the surface snow line by using the $3\ \mu\text{m}$ water ice absorption feature in the scattered light if we have a good enough spatial resolution. This method implicitly assumes the presence of water ice particles at the $3\ \mu\text{m}$ disk surface. However, an efficient photodesorption may remove the particles from the surface and the absorption feature from the scattered radiation. On the other hand, Honda et al. (2009) detected the absorption feature in the scattered light from

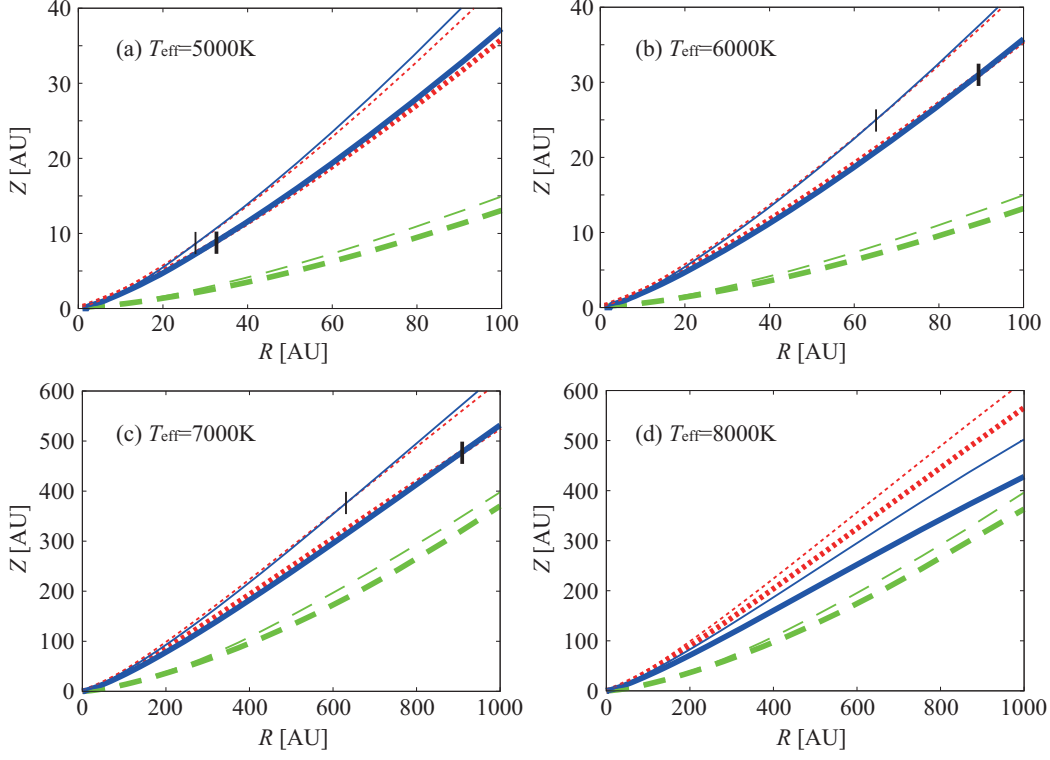


Figure 4. Same as Figure 3, but for various stellar effective temperatures. The thick and thin curves are the cases with and without the water ice opacity, respectively. Note that there is a difference in the axis scales between the panels (a) and (b) and the panels (c) and (d).

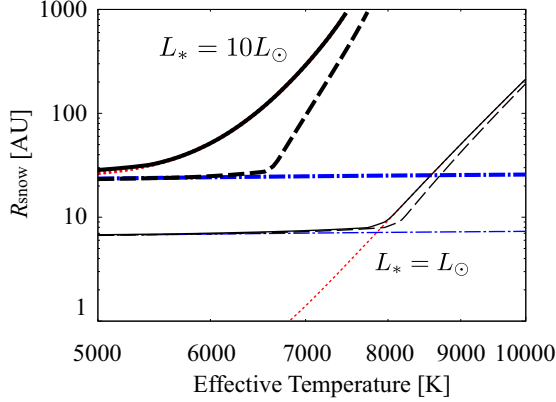


Figure 5. Position of the surface snow line as a function of stellar effective temperature with the stellar mass of $1 M_{\odot}$. The horizontal and vertical axes represent the effective temperature and the position of the surface snow line, respectively. The thick and thin curves show different stellar luminosities as indicated in the panel. The dot-dashed curves show the snow line position where the equilibrium between sublimation and condensation is established. The dotted curves show the position where the equilibrium between photodesorption and condensation is established. The solid curves show the position determined by the equilibrium among photodesorption, condensation, and sublimation. The dashed curves are the same as the solid curves but without the stellar UV excess.

the outer disk at $R \gtrsim 140$ AU of HD142527, although they did not resolve the snow line position because of insufficient spatial resolution. Therefore, photodesorption does not remove water ice particles completely from the disk surface of HD142527.

As found in §3.2.1, photodesorption surpasses sublimation at the disk surface and R_{snow} is determined by the balance between photodesorption and condensation when T_* exceeds a certain value which is defined as

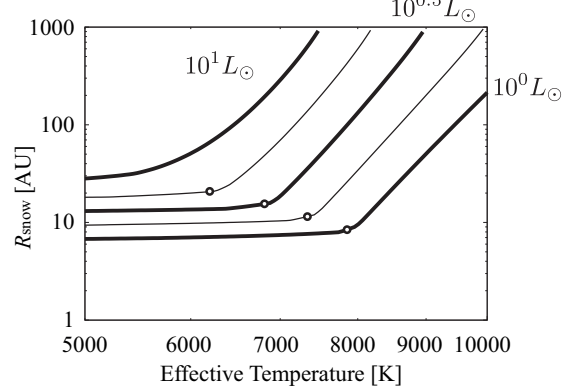


Figure 6. Same as Figure 5, but for various stellar luminosities. The open circles indicate the critical temperatures T_c defined in §3.2.

the critical temperature T_c . This temperature also depends on L_* as found in §3.2.2. Let us over-plot the boundaries at which the mechanism determining R_{snow} changes from the sublimation–condensation balance to the photodesorption–condensation balance on the HR diagram and compare them with Herbig Ae/Be stars on the diagram (Fig. 8). In particular, HD142527, where the water ice feature in the scattered light was detected, is the key object in this comparison. In addition, we also examine effects of other parameters such as photodesorption yield, H_2O abundance, etc. on the boundaries.

As a reference, we define the fiducial model where $M_* = 3 M_{\odot}$, the surface density at 1 AU $\Sigma_{1\text{AU}} = 1700 \text{ g cm}^{-2}$, the total (vapor+ice) number fraction of water $X_{\text{total}}^{\text{H}_2\text{O}} = 1.2 \times 10^{-3}$, and the photodesorption yield $Y_{\text{pd}} = 1 \times 10^{-3}$. In addition, we consider three other

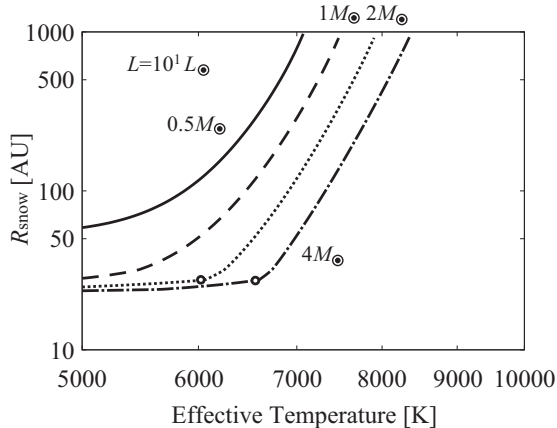


Figure 7. Same as Figure 5, but for various stellar masses. The stellar luminosity of $10 L_{\odot}$ is assumed. The solid, dashed, dotted, and dot-dashed curves show the surface snow line position with the stellar mass of $0.5 M_{\odot}$, $1 M_{\odot}$, $2 M_{\odot}$, and $4 M_{\odot}$, respectively. The open circles indicate the critical temperatures T_c defined in §3.2.

models: A, B, and C, where $X_{\text{total}}^{\text{H}_2\text{O}}$ is increased by a factor of 2, Y_{pd} is reduced by a factor of 2, and $X_{\text{total}}^{\text{H}_2\text{O}}$ is increased by a factor of 2 and Y_{pd} is reduced by a factor of 2, respectively (Table 1). In Figure 8, we show the boundaries of these models by the dotted lines with the labels like ‘fiducial’ on the HR diagram. Interestingly, the boundaries of the models A and B are completely overlapped. The reason is the offset of twice $X_{\text{total}}^{\text{H}_2\text{O}}$ in the model A and half Y_{pd} in the model B as shown in §4.2 analytically. In Figure 8, we also show the evolution tracks of pre-main sequence stars with various stellar masses from Yi et al. (2001) (solid lines with labels of M_*) and the stellar parameters of the observed Herbig Ae/Be stars from van Boekel et al. (2005) (circles). HD142527 is indicated by the square.

In the upper-left region from the boundaries in Figure 8, the photodesorption–condensation balance determines R_{snow} . On the other hand, in the lower-right region from the boundaries, the sublimation–condensation balance determines it. In the photodesorption–condensation case, the surface snow line moves outward significantly as shown in §3.2. Since Honda et al. (2009) detected ice particles on the disk surface at $R \gtrsim 140$ AU of HD142527, we expect that HD142527 is in the sublimation–condensation area. However, it is in the photodesorption–condensation area for the fiducial model. On the other hand, this object is in the sublimation–condensation area for the model C and marginally for the models A and B.

Even if the surface snow line is controlled by photodesorption, it is possible that $R_{\text{snow}} < 140$ AU as shown in Figures 5 and 6. Then, we show the boundaries at which $R_{\text{snow}} = 100$ AU on the HR diagram in Figure 9. The solid lines with labels fiducial, A/B, and C are the boundaries for the four models in Table 1. We also show the boundary of 1000 AU for the fiducial model as the dashed line for a comparison. We find HD142527 between the boundaries of 100 AU for the fiducial and A/B models. In fact, this object is on the boundary of 300 AU for the fiducial model which is not shown in Figure 9. Given the uncertainty of our simple model, we conclude that R_{snow} in the HD142527 disk is 100–300 AU which is still consistent with the observations by Honda et al. (2009).

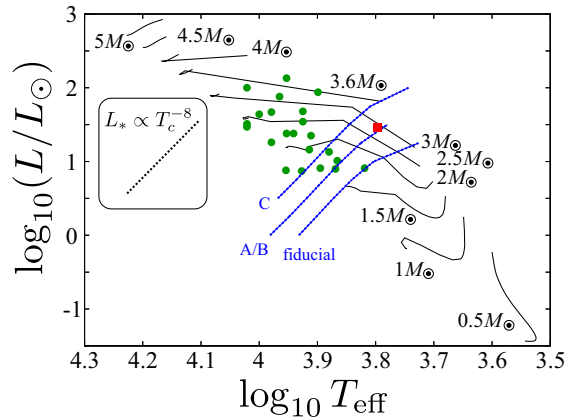


Figure 8. Boundaries (dotted lines with fiducial, A/B, and C) at which the mechanism determining the position of the surface snow line changes. In the upper left side from the boundaries, the mechanism is the balance between photodesorption and condensation. In the lower right side, the mechanism is the balance between sublimation and condensation. The labels fiducial, A/B, and C correspond to the models summarized in Table 1. Note that the models A and B are completely overlapped. The inset shows the slope of the boundaries analytically derived in §4.2. The solid curves with labels of the stellar mass show the evolution tracks of pre-main sequence stars from Yi et al. (2001). The circles are the stellar parameters of the Herbig Ae/Be stars from van Boekel et al. (2005). The square shows HD142527 observed by Honda et al. (2009).

On the other hand, there are many Herbig Ae/Be stars in the upper-left region far from the boundaries of 100 AU and even 1000 AU in Figure 9. Photodesorption is probably very efficient for these objects, and water ice particles disappear from the surface of the disk around the objects. Then, we expect that there is not the $3 \mu\text{m}$ water ice feature in the scattered light from the disks. This will be an observational test to examine whether photodesorption is active or not on the disk surface.

Finally we note a possible caveat in resolving the surface snow line by using the water ice $3 \mu\text{m}$ feature in the scattered light. As found in Figure 4, the ice-condensation front and the $3 \mu\text{m}$ surface (i.e. $\tau_{3\mu\text{m}} = 1$ layer) are always close to each other when $T_* \lesssim T_c$. When we are moving from the outer disk to the inner one on the scattered light image, thus, the strength of the $3 \mu\text{m}$ feature may not disappear suddenly at the surface snow line, but may weaken gradually. In other words, the surface snow line is not a ‘clear’ line. In order to predict the change of the feature strength, we need to simulate observations, which would be a future work.

4.2. Analytic expression of the critical effective temperature

Here we try to derive an analytic formula describing the critical temperature, T_c . The mechanism determining R_{snow} changes depending on T_* ; if $T_* < T_c$, it is the balance between condensation and sublimation, whereas if $T_* > T_c$, it is the balance between condensation and photodesorption. Thus, equation (2) can be approximated to

$$\begin{cases} \dot{s}_{\text{con}} + \dot{s}_{\text{sub}} \approx 0 & (T_* < T_c) \\ \dot{s}_{\text{con}} + \dot{s}_{\text{pd}} \approx 0 & (T_* > T_c) \end{cases} \quad (8)$$

When $T_* < T_c$, equation (8) becomes $X_{\text{total}}^{\text{H}_2\text{O}} P \approx P_{\text{sat}}$, where $X_{\text{total}}^{\text{H}_2\text{O}}$ is the number fraction of H_2O molecules

Table 1
Parameters for the (T_c, L_*) curves in Figures 8 and 9.

Model	$\Sigma_{1\text{AU}}$ (g cm $^{-2}$)	M_* (M_\odot)	$X_{\text{total}}^{\text{H}_2\text{O}}$	Y_{pd}
fiducial model	1700	3	1.2×10^{-3}	1.0×10^{-3}
A	1700	3	2.4×10^{-3}	1.0×10^{-3}
B	1700	3	1.2×10^{-3}	0.5×10^{-3}
C	1700	3	2.4×10^{-3}	0.5×10^{-3}

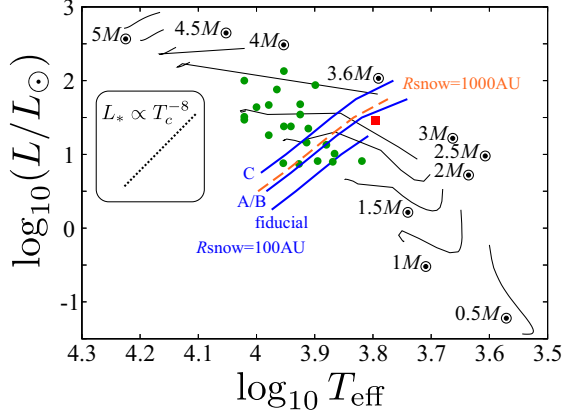


Figure 9. Same as Figure 8, but the solid lines with fiducial, A/B, and C are the sets of the stellar luminosity and effective temperature which give the position of the surface snow line $R_{\text{snow}} = 100$ AU. The dashed line is the sets which give $R_{\text{snow}} = 1000$ AU for the fiducial model.

relative to all gas particles, P and P_{sat} are the gas pressure and the saturation pressure of water vapor, respectively (see eqs. [B1–B5]). We have assumed that the vapor fraction $X_{\text{vapor}}^{\text{H}_2\text{O}} \sim X_{\text{total}}^{\text{H}_2\text{O}}$. The saturation pressure is a rapid function of gas temperature T . Thus, $X_{\text{total}}^{\text{H}_2\text{O}} P \approx P_{\text{sat}}$ is established only when $T \simeq 100$ K on the disk surface. This means that R_{snow} is the position where the dust temperature becomes $T \simeq 100$ K. The dust temperature on the disk surface is determined by $\sigma T^4 \approx L_*/4\pi R^2$. For a fixed T , we obtain R_{snow} determined by the condensation–sublimation balance as

$$R_{\text{snow,sub}} \propto L_*^{1/2}. \quad (9)$$

This relation is very consistent with the dot-dashed lines in Figure 5.

When $T_* > T_c$, equation (8) becomes $Y_{\text{pd}} N_{\text{abs}} \propto X_{\text{total}}^{\text{H}_2\text{O}} \rho$, where Y_{pd} is the photodesorption yield, N_{abs} is the number flux of FUV photons absorbed by water ice grains, and ρ is the gas mass density (see eqs. [B4–B6]). The FUV number flux N_{abs} given by equation (B7) can be approximated to $N_{\text{abs}} \propto L_* T_*^6 R^{-2}$ for a fixed L_* when the FUV absorption efficiency parameter (ratio of the absorption and geometrical cross sections of grains) $Q_{\text{abs}} \sim 1$ and the stellar FUV excess is omitted. The gas density ρ should be that at the $3 \mu\text{m}$ surface: $\rho_{3\mu\text{m}} = \rho(\tau_{3\mu\text{m}} = 1)$. This can be approximated to $\rho_{3\mu\text{m}} \propto 1/H_{\text{P}} \propto M_*^{1/2} R^{-3/2}$, where H_{P} is the pressure scale-height. We have omitted the R dependence in the equatorial temperature T_0 because T_0 is almost constant at $R \sim 100$ AU (Chiang & Goldreich 1997). Note that $\rho_{3\mu\text{m}}$ is independent of the normalization of the surface mass density Σ because we always see the layer with $\tau_{3\mu\text{m}} = 1$. However, it depends on H_{P} which determines the density profile. As a result, we obtain

$Y_{\text{pd}} L_* T_*^6 R^{-2} \propto X_{\text{total}}^{\text{H}_2\text{O}} M_*^{1/2} R^{-3/2}$, and then, R_{snow} determined by the condensation–photodesorption balance becomes

$$R_{\text{snow,pd}} \propto T_*^{12} L_*^2 Y_{\text{pd}}^2 X_{\text{total}}^{\text{H}_2\text{O}^{-2}} M_*^{-1}, \quad (10)$$

which agrees with the dotted lines in Figure 5.

Finally, we define T_c as T_* when $R_{\text{snow,sub}} = R_{\text{snow,pd}}$. Then we obtain

$$T_c \propto L_*^{-1/8} M_*^{1/12} Y_{\text{pd}}^{-1/6} X_{\text{total}}^{\text{H}_2\text{O}^{1/6}}. \quad (11)$$

Comparing this with the results shown in Figure 8, we obtain

$$T_c = 8500 \text{ K} \left(\frac{L_*}{1 L_\odot} \right)^{-1/8} \left(\frac{M_*}{3 M_\odot} \right)^{1/12} \times \left(\frac{Y_{\text{pd}}}{1 \times 10^{-3}} \right)^{-1/6} \left(\frac{X_{\text{total}}^{\text{H}_2\text{O}}}{1.2 \times 10^{-3}} \right)^{1/6}. \quad (12)$$

This formula would be useful for the readers to expect which balance determines R_{snow} . If $T_* > T_c$, one may expect the balance between condensation and photodesorption. For the opposite case, the balance between condensation and sublimation is expected.

4.3. Effects of processes omitted

4.3.1. Photodissociation

We have omitted photodissociation of H_2O molecules, whereas this process is suggested to be important in disks around Herbig stars (Pontoppidan et al. 2010; Fedele et al. 2011). Here we justify this omission.

The photodissociation rate is given by $k_{\text{pdis}} \approx \sigma_{\text{pdis}} N_{\text{FUV}}$, where σ_{pdis} is the cross section for photodissociation and N_{FUV} is the number flux of FUV photons.² According to Lee (1984), $\sigma_{\text{pdis}} \sim 10^{-18} \text{ cm}^2$ for H_2O molecules. On the other hand, the photodesorption rate is given by $k_{\text{pdes}} \approx \pi s^2 Q_{\text{abs}} Y_{\text{pd}} N_{\text{FUV}}$, where s is the grain size, $Q_{\text{abs}} \sim 1$ is the absorption efficiency parameter, and Y_{pd} is the photodesorption yield. Since the time-scale is $\tau = 1/k$, the ratio of the two time-scales is $\tau_{\text{pdis}}/\tau_{\text{pdes}} = k_{\text{pdes}}/k_{\text{pdis}} \approx \pi s^2 Y_{\text{pd}}/\sigma_{\text{pdis}} \sim 10^7$ for $s \sim 1 \mu\text{m}$ and $Y_{\text{pd}} \sim 10^{-3}$. Then we find that photodissociation is several orders of magnitude slower than photodesorption. Therefore, photodissociation does not affect the balance between photodesorption and condensation.

We may still argue the importance of photodissociation in observations. When photodesorption becomes faster than condensation, water ice particles are finally evaporated. This destruction time-scale is given by $\tau_{\text{dest}} = s/|\dot{s}_{\text{pd}}|$, where \dot{s}_{pd} is the size changing rate by photodesorption (eq. B6). The ratio of this

² N_{abs} in the previous subsection is equal to $Q_{\text{abs}} N_{\text{FUV}}$.

time-scale to the photodissociation one is $\tau_{\text{dest}}/\tau_{\text{pdis}} \approx \sigma_{\text{pdis}}\rho_{\text{ice}}s/(m_{\text{H}_2\text{O}}Y_{\text{pd}}) \sim 10^5$ for $s \sim 1 \mu\text{m}$ and $Y_{\text{pd}} \sim 10^{-3}$ (ρ_{ice} is the ice material density and $m_{\text{H}_2\text{O}}$ is the mass of a H_2O molecule). Thus, when the ice destruction is completed, evaporated H_2O molecules have been already photodissociated. Therefore, we expect that there is no H_2O molecules in gas phase above the disk surface where photodesorption destroys ice particles.

4.3.2. X-ray photodesorption

We have neglected desorption by X-ray (e.g., Najita et al. 2001). The photodesorption rates by X-ray and FUV are given by $k_i \approx \pi s^2 Q_i Y_i N_i$, where i is X-ray or FUV, s is the grain size, Q_i is the absorption efficiency, Y_i is the photodesorption yield, and N_i is the photon number flux. Thus, the ratio is $k_X/k_{\text{FUV}} \approx (Q_X/Q_{\text{FUV}})(Y_X/Y_{\text{FUV}})(N_X/N_{\text{FUV}})$.

X-ray luminosity of Herbig stars is observed in a range of 10^{-7} – 10^{-4} of the bolometric luminosity (Stelzer et al. 2005). Given about two orders of magnitude higher energy per a photon in X-ray than in FUV and that $\sim 10\%$ of the bolometric energy is emitted in FUV for Herbig stars, we obtain $N_X/N_{\text{FUV}} < 10^{-5}$. The X-ray absorption efficiency is $Q_X \sim 10^{-1}$ which is estimated from the sum of atomic photoionization cross sections. Then, we find $Q_X/Q_{\text{FUV}} \sim 10^{-1}$. The yield for X-ray Y_X is uncertain for water ice, while $Y_{\text{FUV}} \sim 10^{-3}$. Najita et al. (2001) estimated $Y_X \sim 10$ – 10^3 for CO from a consideration of ‘spot heating’ of subunits which is hit by a X-ray photon and is poorly connected thermally with other parts in a grain. They estimated $< 0.01 \mu\text{m}$ subgrains, which cover the parent grain, as the subunits. Comparing CO to H_2O , the latter has 5 times larger binding energy than the former (Sandford & Allamandola 1988), which reduces Y_X for H_2O by the same factor. In addition, the connecting ‘neck’ between H_2O ice particles is thicker than that of silica considered in Najita et al. (2001) because of sintering (Sirono 2011), further reducing Y_X because of an enhanced conductivity of heat. Thus, we estimate $Y_X/Y_{\text{FUV}} < 10^5$, although a more detailed study is encouraged. In summary, we obtain $k_X/k_{\text{FUV}} < 10^{-1}$ and we can omit X-ray photodesorption at the disk surface. However, we note that X-ray photodesorption should be important in the disk interior, where $k_X/k_{\text{FUV}} > 1$ because N_{FUV} is significantly smaller than that at the surface.

4.3.3. Dust settling and turbulent mixing

In this paper, we have not considered dust settling and turbulent mixing although they may affect the vertical distribution of water ice particles and the surface snow line. If the dust settling toward the mid-plane occurs, the height of the $3 \mu\text{m}$ surface is reduced. This results in a larger density and a faster condensation at the surface. Thus, the surface snow line moves inward. To estimate the amount of the shift, we need further quantitative studies.

The turbulent mixing may supply water ice particles from the disk interior to the disk surface even if photodesorption removes the particles from the surface. However, the mixing time-scale is 1×10^3 yr at 10 AU and 1×10^4 yr at 100 AU according to Heinzeller et al. (2011), while the destruction time-scale of $1 \mu\text{m}$ ice particles by pho-

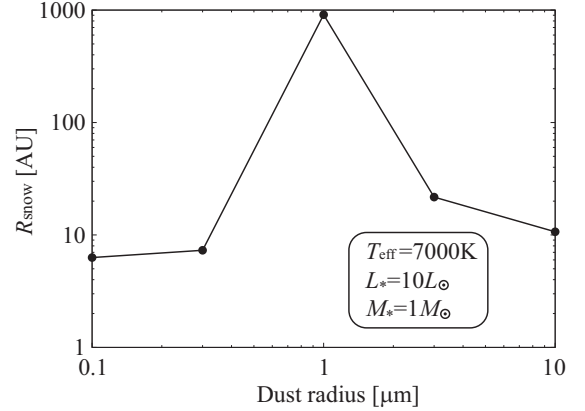


Figure 10. Position of the surface snow line as a function of dust grain size for the case of the effective temperature of 7000 K, the luminosity of $10 L_{\odot}$, and the mass of $1 M_{\odot}$.

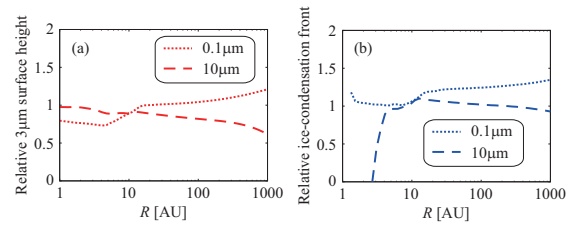


Figure 11. (a) Height of the $3 \mu\text{m}$ surface relative to the $1 \mu\text{m}$ -sized grain case. (b) Height of the ice-condensation front relative to the $1 \mu\text{m}$ -sized grain case. The dotted and dashed lines are the cases of $0.1 \mu\text{m}$ -sized and $10 \mu\text{m}$ -sized grain cases, respectively.

todesorption is 3×10^2 yr at 10 AU and 3×10^3 yr at 100 AU. Therefore, the ice supply by turbulence is not fast enough.

4.3.4. Grain size dependence

Figure 10 shows R_{snow} as a function of dust grain size. We find that R_{snow} depends on the grain size **in a complex way**; the $1 \mu\text{m}$ -sized grain case gives the largest R_{snow} and smaller or larger grain size cases give smaller R_{snow} s. This is because R_{snow} is the cross-point of the two curves, i.e. the ice-condensation front and the $3 \mu\text{m}$ disk surface, which have a similar slope, and it is very sensitive to the relative position of the two curves.

To see the reason of this complex behavior of R_{snow} , we show in Figure 11 (a) the $3 \mu\text{m}$ surface height for the $0.1 \mu\text{m}$ -sized grain and $10 \mu\text{m}$ -sized grain cases relative to the $1 \mu\text{m}$ -sized grain case. The panel (b) shows those of the ice-condensation front. From Figure 11, we find that at around 10 AU, the $3 \mu\text{m}$ surface heights of both of the 0.1 and $10 \mu\text{m}$ -sized cases are lower than that of the $1 \mu\text{m}$ -sized case, while the ice-condensation heights of the both cases are similar to that of the $1 \mu\text{m}$ -sized case. This results in a smaller R_{snow} for the 0.1 and $10 \mu\text{m}$ -sized case than for the $1 \mu\text{m}$ -sized case. This behavior is caused by a complex size dependence of the absorption and scattering opacities with and without water ice. More studies about this point are required in future.

5. SUMMARY

We have investigated the effect of photodesorption on the ice-condensation front and on the surface snow line position in a protoplanetary disk around a Herbig Ae/Be star. This study is inspired by the detec-

tion of an absorption feature of water ice at the wavelength $3 \mu\text{m}$ in the scattered light from the surface of the disk around HD142527 by Honda et al. (2009). We have used 1+1D plane-parallel radiative transfer algorithm by Dullemond et al. (2002) and Inoue et al. (2009) to obtain the temperature and density structure in the disk. Then we have determined the amount of water ice particles by the balance between photodesorption, sublimation, and condensation, following Grigorieva et al. (2007).

We find that the effect of photodesorption depresses the ice-condensation front toward the mid-plane and pushes the surface snow line outward significantly. We also find that the surface snow line position is determined by the balance between photodesorption and condensation for a higher effective temperature of the central star, while it is determined by the balance between sublimation and condensation for a lower effective temperature. We define the switching point of the two balances in the effective temperature as the critical temperature. The surface snow line is located at a small disk radius ($<$ several tens of AU) if the stellar effective temperature is lower than the critical temperature. In the opposite case, the surface snow line moves outward rapidly and tends to be at a large disk radius ($>$ several hundreds of AU) due to efficient photodesorption. We also derive an analytic formula to describe the critical temperature as a function of stellar and disk parameters.

We discuss a few implications for the observation of the surface snow line in circumstellar disks. We plot the critical temperature as a function of the stellar luminosity on the HR diagram. This indicates the boundary between two mechanisms determining the position of the surface snow line: the sublimation–condensation balance and the photodesorption–condensation balance. Most of Herbig Ae/Be stars are found in the photodesorption area. We also plot the line which gives the position of the surface snow line of 100 AU on the HR diagram. HD142527 is found slightly above the line, suggesting the surface snow line of the HD142527 disk is located at 100–300 AU from the central star. This is consistent with the observations by Honda et al. (2009) which indicated the surface snow line was located at < 140 AU. We also find that there are many Herbig Ae/Be stars whose snow line on the disk surface is > 100 AU or even > 1000 AU. It is difficult to detect water ice particles on the surface of the disk around these stars, which will be easily confirmed by observations. Finally, we also find that the surface snow line position depends on the dust grain size by a complex way, which is worth investigating more thoroughly in future.

We thank the referee for her/his constructive comments which were useful to improve the clarity of this manuscript very much.

APPENDIX

DISK STRUCTURE

Here, we introduce details of our calculations to determine the density and temperature structure of a circumstellar disk. Our method is based on Dullemond et al. (2002), Inoue et al. (2009), and Oka, Nakamoto & Ida (2011)

Hydrostatic equilibrium

The dynamical structure of the disk in the vertical direction is assumed to be determined by the balance between the vertical component of the gravitational force by the central star and the gas pressure gradient (hydrostatic equilibrium);

$$\frac{\partial P(R, Z)}{\partial Z} = -\rho(R, Z) \frac{GM_*}{R^3} Z, \quad (\text{A1})$$

where $P(R, Z)$, $\rho(R, Z)$, G , and M_* are the gas pressure, the gas volumetric density, the gravitational constant, and the mass of the central star, respectively. We adopt the equation of state of the ideal gas for the disk gas;

$$P(R, Z) = \frac{\rho(R, Z)}{\mu_{\text{mean}} m_u} kT(R, Z), \quad (\text{A2})$$

where k , $T(R, Z)$, μ_{mean} , and m_u are the Boltzmann constant, the temperature of the disk gas, the mean molecular weight (we set this value to be 2.3), and the atomic mass unit, respectively. To obtain the vertical density profile $\rho(R, Z)$ at a radius R by integrating equation (A1) with (A2) along the vertical axis Z , we need the mid-plane density $\rho(R, 0)$ as the normalization of $\rho(R, Z)$. This is given by equating the surface density $\Sigma(R)$ with the integral of $\rho(R, Z)$ along Z as

$$\Sigma(R) = \int_{-\infty}^{\infty} \rho(R, Z) dZ. \quad (\text{A3})$$

The surface density $\Sigma(R)$ is given by equation (1).

Radiative transfer

The temperature in the disk is determined by the balance between the cooling and heating. The disk is heated by the irradiation from the central star. We ignore the heating by the viscous dissipation of the disk gas, because the snow line at the disk surface is located at relatively outer part of the disk where the viscous heating is negligibly small compared with the heating by the irradiation of the central star. The cooling rate in the disk is determined by the radiation energy transfer and the convection is not taken into account because of the low density in the disk.

Assuming a plane-parallel structure along the Z -axis in an annulus at a certain R , the equation of the radiative transfer is given by

$$\mu \frac{dI_{\mu,\nu}(Z)}{dZ} = \rho\kappa_\nu(S_\nu(Z) - I_{\mu,\nu}(Z)), \quad (\text{A4})$$

where μ , ν , $I_{\mu,\nu}$, κ_ν , and S_ν are the cosine of the angle between the propagation direction and the Z -axis, the frequency, the specific intensity, the extinction coefficient, and the source function, respectively. The subscripts μ and ν of each quantity represent the direction cosine and the frequency of that quantity. If we assume an isotropic scattering and local thermodynamics equilibrium, the source function S_ν is given by

$$S_\nu(Z) = (1 - \varpi_\nu(Z))B_\nu(T) + \varpi_\nu(Z) \frac{1}{2} \int_{-1}^1 I_{\mu,\nu} d\mu + \varpi_\nu(Z) \frac{F_{\text{irr},\nu}(Z)}{4\pi}, \quad (\text{A5})$$

where ϖ_ν , $B_\nu(T)$, and $F_{\text{irr},\nu}(Z)$ are the single scattering albedo, Planck function with temperature T , and radiation flux from the central star, respectively.

We evaluate $F_{\text{irr},\nu}(Z)$ using the so-called grazing angle recipe (e.g., Chiang and Goldreich 1997, Dullemond et al. 2002) as

$$F_{\text{irr},\nu}(Z) = \frac{L_\nu}{4\pi R^2} \exp\left(-\frac{\tau_\nu(R, Z)}{\beta}\right), \quad (\text{A6})$$

where β , L_ν , and $\tau_\nu(R, Z)$ are the grazing angle (i.e. incidence angle of the radiation from the central star into the disk surface), the luminosity of the central star, and the optical depth between a point (R, Z) and the infinity along the vertical direction (R, ∞) , respectively. In this study, we set $\beta = 0.05$ throughout of the disk for simplicity which is a typical value of the grazing angle. We assume that the central star emits the black body radiation with an effective temperature T_* . Hence, $L_\nu = 4\pi^2 R_*^2 B_\nu(T_*)$, where R_* is the radius of the photosphere of the central star. The optical depth τ_ν is defined as

$$\tau_\nu(R, Z) = \int_Z^\infty \kappa_\nu \rho(R, Z) dZ. \quad (\text{A7})$$

The temperature of the dust particles are determined by the assumption of the radiative equilibrium;

$$q_{\text{irr}} + \int_0^\infty \rho\kappa_\nu(1 - \varpi_\nu) \oint I_{\mu,\nu}(\boldsymbol{\Omega}) d\Omega d\nu = 4\pi \int_0^\infty \rho\kappa_\nu(1 - \varpi_\nu) B_\nu(T) d\nu, \quad (\text{A8})$$

where q_{irr} is the heating rate by the irradiation of the central star and given by

$$q_{\text{irr}} = \int_0^\infty \rho(Z)\kappa_\nu(1 - \varpi_\nu) F_{\text{irr},\nu}(Z) d\nu. \quad (\text{A9})$$

We can obtain the diffuse radiation field $I_{\mu,\nu}$, the temperature of the dust particles T , and the source function $S_\nu(T)$ by solving equations (A4) and (A8) iteratively. Since a straight forward way to solve these equations converges very slowly, we employ a variable Eddington factor method (e.g., Dullemond et al. 2002; Inoue et al. 2009) for a rapid convergence.

RATES FOR SUBLIMATION, CONDENSATION, AND PHOTODESORPTION

Here, we describe the changing rates of the radius of water ice particles by sublimation, condensation, and photodesorption. These rates are according to Grigorieva et al. (2007).

The decreasing rate of the radius of water ice particles due to sublimation \dot{s}_{sub} is given by

$$\dot{s}_{\text{sub}} = -\frac{\dot{m}_{\text{sub}}}{4\pi\rho_{\text{ice}}s^2} = -\frac{\eta\Phi_{\text{sub}}}{\rho_{\text{ice}}} \quad (\text{B1})$$

$$\Phi_{\text{sub}} = 4.08 \times 10^{-2} \left(\frac{P_{\text{sat}}}{1\text{torr}}\right) \left(\mu_{\text{H}_2\text{O}} \frac{1\text{K}}{T}\right) \text{g cm}^{-2}\text{s}^{-1}, \quad (\text{B2})$$

where \dot{m}_{sub} is the decreasing rate of the grain mass, s is the grain radius, ρ_{ice} is the density of water ice, Φ_{sub} is the mass sublimation rate, P_{sat} is the saturated water vapor pressure, η is the covering factor (fraction of the surface covered by sublimating material), and $\mu_{\text{H}_2\text{O}}$ is the atomic weight of the water molecule. We set ρ_{ice} to be 0.92 g cm^{-3} as Miyake & Nakagawa (1993) and consider that there exists purely icy dust particles ($\eta = 1$). We adopt the saturated water vapor pressure same as Grigorieva et al. (2007):

$$P_{\text{sat}} = \begin{cases} 2.67 \times 10^{10} \exp\left(-\frac{6141.667\text{K}}{T}\right) \text{ torr} & (T \geq 170\text{K}), \\ 5.69 \times 10^{12} \exp\left(-\frac{7043.51\text{K}}{T}\right) \text{ torr} & (T < 170\text{K}). \end{cases} \quad (\text{B3})$$

The increasing rate of the radius of water ice particles due to condensation is given by substituting the partial pressure of water vapor $P_{\text{H}_2\text{O}}$ for the saturated water vapor pressure P_{sat} in equation (B2). Namely,

$$\dot{s}_{\text{con}} = \frac{\dot{m}_{\text{con}}}{4\pi\rho_{\text{ice}}s^2} = \frac{\eta\Phi_{\text{con}}}{\rho_{\text{ice}}}, \quad (\text{B4})$$

$$\Phi_{\text{con}} = 4.08 \times 10^{-2} \left(\frac{P_{\text{H}_2\text{O}}}{1 \text{ torr}} \right) \left(\mu_{\text{H}_2\text{O}} \frac{1 \text{ K}}{T} \right) \text{ g cm}^{-2} \text{ s}^{-1}, \quad (\text{B5})$$

where \dot{m}_{con} and Φ_{con} are the increasing rate of the grain mass and the mass condensation rate onto the grains, respectively. The partial pressure of water vapor $P_{\text{H}_2\text{O}}$ is given by the product of the number fraction of water vapor $X_{\text{H}_2\text{O},\text{vapor}}$ and the gas pressure P .

The decreasing rate of the radius of water ice particles due to photodesorption is given by:

$$\dot{s}_{\text{pd}} = - \frac{\eta m_{\text{H}_2\text{O}} Y_{\text{pd}} N_{\text{abs}}}{4 \rho_{\text{ice}}} \quad (\text{B6})$$

where $m_{\text{H}_2\text{O}} = 3 \times 10^{-23}$ g is the mass of a water molecule, Y_{pd} is the photodesorption yield, and N_{abs} is the number flux of the FUV radiation absorbed by ice particles. $N_{\text{abs}}(R, Z)$ is given by

$$N_{\text{abs}}(R, Z) = \int_{\lambda_{\text{min}}}^{\lambda_{\text{max}}} \frac{F_{\lambda}(R, Z)}{hc/\lambda} Q_{\lambda}^{\text{abs}} d\lambda, \quad (\text{B7})$$

where $F_{\lambda}(R, Z)$ is the incident FUV flux of the wavelength λ at the position (R, Z) , and Q_{λ}^{abs} is the absorption coefficient for water ice particles. We set the wavelength range of the integral of equation (B7) same as Grigorieva et al. (2007): $\lambda_{\text{min}} = 0.091 \mu\text{m}$ (13.6 eV) and $\lambda_{\text{max}} = 0.24 \mu\text{m}$ (5.1 eV).

Westley et al. (1995a,b) experimentally investigated the photodesorption of water ice and derived the yield as $Y_{\text{pd}} \sim 1.0 \times 10^{-3}$. Andersson et al. (2006) and Andersson & van Dishoeck (2008) carried out a classical molecular dynamics simulation of photodesorption and derived the yield consistent with Westley et al. (1995a,b). The weakness of their study was that their calculation was operated with a limited temperature and a limited wavelength range of the UV radiation. The latest experimental study on the photodesorption is Öberg et al. (2009). They experimentally determined the rate of the photodesorption of water ice eliminating influences by other mechanisms and equipments, and obtained more detailed yield as a function of temperature and the thickness of the molecular layer of water ice as $Y_{\text{pd}}(T, x > 8) = 10^{-3}(1.3 + 0.032T)$ UV photon⁻¹. However, the results of these experimental and theoretical studies about photodesorption yield still have a large uncertainty. We set Y_{pd} to be 1×10^{-3} as Dominik et al. (2005) and Grigorieva et al. (2007) as the fiducial case.

REFERENCES

- Aikawa, Y., & Herbst, E. 1999, *A&A*, 351, 233
Aikawa, Y., van Zadelhoff, G. J., van Dishoeck, E. F., & Herbst, E. 2002, *A&A*, 386, 622
Aikawa, Y. 2007, *ApJ*, 656, L93
Andersson, S., Al-Halabi, A., Kroes, G.-J., & van Dishoeck, E. F. 2006, *J. Chem. Phys.*, 124, 4715
Andersson, S., & van Dishoeck, E. F. 2008, *A&A*, 491, 907
Asplund, M., Grevesse, N., Sauval, A. J., & Scott, P. 2009, *ARA&A*, 47, 481
Bergin, E. A., et al. 2010, *A&A*, 521, L33
Bethell, T., Bergin, E. 2011, *ApJ*, 739, 78
Chiang, E. I., & Goldreich, P. 1997, *ApJ*, 490, 368
Davis, S., S. 2005, *ApJ*, 620, 994
Dodson-Robinson, S. E., Willacy, K., Bodenheimer, P., Turner, N. J., & Beichman, C. A. 2009, *Icarus*, 200, 672
Dominik, C., Ceccarelli, C., Hollenbach, D., & Kaufman, M. 2005, *ApJ*, 635, L85
Dullemond, C. P., & Dominik, C. 2004, *A&A*, 421, 1075
Dullemond, C. P., van Zadelhoff, G. J., & Natta, A. 2002, *A&A*, 389, 464
Fedele, D., Pascucci, I., Brittain, S., Kamp, I., Woitke, P., Williams, J. P., Dent, W. R. F., Thi, W.-F. 2011, *ApJ*, 732, 106
Fogel, J. K. J., Bethell, T. J., Bergin, E. A., Calvet, N., & Semenov, D. 2011, *ApJ*, 726, 29
Grigorieva, A., Thébault, P., Artymowicz, P., & Brandeker, A. 2007, *A&A*, 475, 755
Habing, H. J., 1968, *Bulletin of the Astronomical Institutes of the Netherlands*, 19, 421
Hama, T., Yokoyama, M., Yabushita, A., Kawasaki, M., Andersson, S., Western, C. M., Ashfold, M., N., R., Dixon, R. N., & Watanabe, N., 2010, *JChPh*, 132, 164508
Hayashi, C. 1981, *Prog. Theor. Phys. Suppl.*, 70, 35
Heinzeller, D., Nomura, H., Walsh, C., & Millar, T. J. 2011, *ApJ*, 731, 115
Herczeg, G. J., Wood, B. E., Linsky, J. L., Valenti, J. A., & Johns-Krull, C. M. 2004, *ApJ*, 607, 369
Hollenbach, D., Kaufman, M. J., Bergin, E. A., & Melnick, G. J. 2009, *ApJ*, 690, 1497
Honda, M., Inoue, A. K., Fukagawa, M., Oka, A., Nakamoto, T., Ishii, M., Terada, H., Takato, N., Kawakita, H., Okamoto, Y. K., Shibai, H., Tamura, M., Kudo, T., & Itoh, Y. 2009, *ApJ*, 690, L110
Inoue, A. K., Honda, M., Nakamoto, T., & Oka, A. 2008, *PASJ*, 60, 557
Inoue, A. K., Oka, A., & Nakamoto, T. 2009, *MNRAS*, 393, 1377
Lee, L. C. 1984, *ApJ*, 282, 172
Malfait, K., Waelkens, C., Bouwman, J., de Koter, A., Eaters, L. B. F. M. 1999, *A&A*, 345, 181
Min, M., Dullemond, C. P., Kama, M., & Dominik, C. 2011, *Icarus*, 212, 416
Miyake, K., Nakagawa, Y. 1993, *Icarus*, 106, 20
Najita, J., Bergin, E. A., & Ullom, J. N. 2001, *ApJ*, 561, 880
Öberg, K. I., Linnartz, H., Visser, R., & van Dishoeck, E. F. 2009, *ApJ*, 693, 1209
Oka, A., Nakamoto, T., & Ida, S. 2011, *ApJ*, 738, 141
Pontoppidan, K. M., Salyk, C., Blake, G. A., Meijerink, R., Carr, J. S., Najita, J. 2010, *ApJ*, 720, 887

- Sandford, S. A., & Allamandola, L. J. 1988, *Icarus*, 76, 201
- Sirono, S. 2011, *ApJ*, 735, 131
- Stelzer, B., Flaccomio, E., Montmerle, T., Micela, G., Sciortino, S., Favata, F., Preibisch, T., & Feigelson, E. D. 2005, *ApJS*, 160, 557
- Sturm, B., et al. 2010, *A&A*, 518, L129
- Terada, H., Tokunaga, A. T., Kobayashi, N., Takato, N., Hayano, Y., & Takami, H. 2007, *ApJ*, 667, 303
- Westley, M. S., Baragiola, R. A., Johnson, R. E., & Baratta, G. A. 1995, *Planet. Space Sci.*, 43, 1311
- Westley, M. S., Baragiola, R. A., Johnson, R. E., & Baratta, G. A. 1995, *Nature*, 373, 405
- Valenti, J. A., Fallon, A. A., Johns-Krull, C. M. 2003, *ApJS*, 147, 305
- van Boekel, R., Min, M., Waters, L. B. F. M., de Koter, A., Dominik, C., van den Ancker, M. E., & Bouwman, J. 2005, *A&A*, 437, 189
- van Kempen, T. A., et al. 2010, *A&A*, 518, L128
- Yi, S., Demarque, P., Kim, Y., Lee, Y., Ree, C. H., Lejeune, T., & Barnes, S. 2001, *ApJS*, 136, 417